INSTITUTE OF PLASMA PHYSICS

NAGOYA UNIVERSITY

Caotic Magnetic Field Line In Toroidal Plasmas

T. Hatori, H. Irie, Y. Abe and K. Urata

(Received — May 9, 1989)

IPPJ-911 May 1989

RESEARCH REPORT

NAGOYA, JAPAN

Caotic Magnetic Field Line
In Toroidal Plasmas

Tadatsugu Hatori, Haruyuki Irie*
Yoshihiko Abe and Kazuhiro Urata

(Received - May 9, 1989)

IPPJ-911 May 1989

Further communication about this report is to be sent to the Research Information Center, Institute of Plasma Physics, Nagoya University, Nagoya 464-01 Japan.

---

* Department of Physics, College of Science and Tecknology, Nihon University, Tokyo 101

Abstract

This is an introductory review of chaotic magnetic field line in plasmas, together with some new results, with emphasis on the long-time tail and the fractional Brownian motion of the magnetic field line. The chaotic magnetic field line in toroidal plasmas is a typical chaotic phenomena in the Hamiltonian dynamical systems. The onset of stochasticity induced by a major magnetic perturbation is thought to cause a macroscopic rapid phenomena called the current disruption in the tokamak discharges. Numerical simulations on the basis of magnetohydrodynamics reveal in fact the disruptive phenomena. Some dynamical models which include the area-preserving mapping such as the standard mapping, and the two-wave Hamiltonian system can model the stochastic magnetic field. Theoretical results with use of the functional integral representation are given regarding the long-time tail on the basis of the radial twist mapping. It is shown that application of renormalization group technique to chaotic orbit in the two-wave Hamiltonian system proves decay of the velocity autocorrelation function with the power law. Some new numerical results are presented which supports these theoretical results.

§1. Introduction

There are a variety of nonlinear phenomena in plasmas including chaotic effects with low degrees of freedom. Especially, problems of conservative dynamical system play an important role in the recent high temperature confined plasmas. Among these, chaotic motion of a single charged particle in a given static and / or high frequency fields, and also the spatially braided structure of magnetic field, are typical two examples. The present article lays stress on the statistical properties of chaotic magnetic field.

A conventional problem of nonlinear oscillation in the plasma physics is a single particle motion in the static magnetic mirror configuration. The mirror geomety is shown in Fig. 1, in which lines of force with arrows are bunched in the regions near the points A and B, so the magnitude of the magnetic field has a well. A charged paticle gyrates locally with cyclotron frequency ω_c around a line of force. Guiding center of the particle bounces along the line between the two turning points A and B, with the bounce frequency ω_b. Cross section of the guiding center through the midplane M drifts across the line of force due to the weak inhomogeniety of the magnetic field. The Poincare plots lie ordinarily on a closed line (dotted line in Fig. 1) after many times of bouncing. The frequency ω_d of drifting motion along the closed curve is called drift frequency. Except for the extraordinary case the following inequalities hold between these three characteristic frequencies ω_c, ω_b and ω_d ,

$$\omega_c \gg \omega_b \gg \omega_d \,. \tag{1.1}$$

Chaotic behaviors originate from the resonance condition,

$$m\omega_c + n\omega_b + p\omega_d = 0 , \tag{1.2}$$

where m, n and p are integers. The three characteristic quasi-periodic motions have three action variables, the magnetic moment μ, longitudinal invariant J and anglar momentum P_ϕ, which are all adiabatic invariants. In the case of fast resonance, $m\omega_c + n\omega_b = 0$, only μ and J change, retaining P_ϕ and total kinetic energy. To the purpose of quantitative study of long-time variation in μ, Chirikov derived a linearized mapping commonly called the standard mapping[1], which describes the jump from (μ, θ) to ($\bar{\mu}$, $\bar{\theta}$) after a half bouncing period, in the form

$$\left.\begin{aligned} \bar{P} &= P + K\sin\theta , \\ \bar{\theta} &= \theta + \bar{P} \quad . \end{aligned}\right\} \tag{1.3}$$

Here θ is the gyration angle, P the scaled deviation of the magnetic moment about a resonant value, and K a parameter characterizing the intensity of the jump in μ. It has been found[2] that the results from Eq.(1.3) agrees well with the calculations based upon the more precise differential equation. A recent study of the standard mapping has been reported[3]. The model (1.3) is applicable also to the study of magnetic lines of force. Slow diffusion processes due to the multiple resonance or the Aronld diffusion also play an important role on the diffusion loss of plasma particles across the magnetic fields.

The main subject of the present article is the chaotic structure of the magnetic line of force in toroidal plasmas. In the magnetic mirror configuration the line of force is

open to the vacuum wall and goes out across it. In the toroidal case, magnetic lines of force are all confined in the toroidal vacuum region. The most standard toroidal device is the tokamak which has been extensively studied for many years. The tokamak configuration is illustrated in Fig 2(a). The inductive electric field along the strong toroidal magnetic field $\vec{B}_t$ drives the current I in the plsma, which produces the poloidal magnetic field $\vec{B}_p$. The resultant magnetic field, $\vec{B}_t + \vec{B}_p$, is shown in Fig.2(b). A typical line starting from a point P_1 goes around the symmetry axis and comes back to the cross section point P_2 through the poloidal surface (shaded surface in Fig.2(b)) to which the initial point P_1 belongs. The angle P_1 O P_2 is called the rotational transform angle, ι. If we trace further the magnetic line of force, it comes back again to P_3 on the same circle centered at O with the same rotational transform angle ι. A set of all points { P_1, P_2, ...P_∞ } are distributed ergodically on the same circle, thus constitue a magnetic surface. Any line of force ergodically covers a magnetic surface except a dense set of surfaces where the rotational transform angle is occasionally a value of 2πn/m,n and m being integers. In the latter case any line of force on the surface, called rational surface, is closed after m turns around the torus and n turns around the toroidal magnetic axis. The reason why all the magnetic field lines in tokamak are confined to a set of nested toroidal magnetic surfaces is the following. To contain the plasma for a long time, it must be in an equilibrium state, in which the Lorentz force balances the pressure gradient of plasma;

$$\nabla p = \frac{1}{c} \vec{J} \times \vec{B} \ . \tag{1.4}$$

Note that the terminology equilibrium does not mean the thermal equilibrium but the force-balanced state. The equation (1.4) imposes a constraint,

$$\vec{B} \cdot \nabla p = 0 \tag{1.5}$$

which says that a magnetic field line must lie on a constant pressure surface to be consistent with the equilibrium condition (1.4). If the equilibrium is unstable to a certain instability, the plasma stays no more in the equilibrium state and does not obey the balance relation (1.4), Therefore the magnetic field line does not necessarily lie on a torus. If the points of intersection of a field line in a poloidal surface cover a finite area rather than lie on a curve, then the field line is called stochastic. The phenomena of magnetic chaos caused by instabilities is described in §2 in details. In §3, it is shown that the equation for the magnetic field line can be described by the Hamiltonian system. The magnetic surface is nothing else than the KAM torus in the terminology of mathematics. The standard mapping (1.3) is applicable to study approximately the chaotic magnetic structure. It should be noted that the absence of magnetic monopole in our world (div $\vec{B}$=0) assures the precise Hamiltonian system for the magnetic field, although the Newton's mechanics for a chaged particle in electromagnetic fields have to suffer from slightly dissipative disturbance which makes the dynamics not so precise Hamiltonian system.

Two chaotic phenomena presented above have a common feature that dynamical variables are bounded throughout the whole evolution process. The motion in the mirror field has three characteristic frequencies and the position of the particle is always confined in a limited region of three dimensional space even in the case of stochastic orbit. The magnetic line of force having two periods, toroidal and poloidal, is confined in the toroidal region. The boundedness of dynamical variables is always accompanied by the stochastic motion if a parameter indicating the nonlinearity is above a threshold value.

After the introductory sections 1 through 3, the remaining sections are contributed to describe the original works by the authors, laying stress on the topics of long-time tail or the algebraic decay of correlation function. This is the result of selfsimilar structure in phase space. In §4, it is shown that turbulent diffusion coefficient for the chaotic orbit in the radial twist mapping relaxes as $t^{-1/2}$ to a certain value, except for the case of the standard mapping.[4] Section 5 deals with analytical prediction of algebraic decay of velocity autocorrelation function in the two-wave Hamiltonian in a similar manner to the renormalization group technique.[5] Section 6 is devoted to show same unpublished new results about the fractional Brownian motion of magnetic field line and the associated anomalous electron transport in plasmas. Finally, a summary and a discussion are given in section 7.

§2. Current disruption observed in Tokamaks and computer simulations

Many works of the standard type dealing with physics of chaos often start with any paradigm dynamical system and end without referring any experimentally observed phenomena. The present magnetic chaos, however, is strongly correlated to a distinct macroscopic phenomena in toroidal plasmas. Among such phenomena, the current disruption observed in tokamaks is the most prominent and dangerous instability. It might be honest to say that any real plasma phenomena cannot completely be described by a single fundamental process. The current disruption might be the case. The onset of magnetic stochasticity is commonly thought to trigger strongly the subsequent unlimitted growth of perturbation or the development of turbulent stage. It is obviously impossible to observe directly the magnetic structures in the high temperature plasmas with any advanced diagnostic tools. Thus the complementary approach through direct numerical integration of the magnetohydrodynamical (MHD) system is useful to obtain the magnetic structure. The MHD simulation to this purpose has first been performed by B. Carreras et al. in 1980[6], and some subsequent simulations have followed. The present article describes some results obtained by ourselves.

A) Current disruption observed in tokamaks

There are a variety of types in the tokamak current disruption. A standard sequence, however, is the following.

Figure 3 shows the obseved time sequences of three quantities before, during and after the disruption[7]. The signal of the soft X-rays in Fig.3 indicates the central electron temperature. It executes the sawtooth oscillations before disruption (stage 1). This small oscillation is sometimes called internal disruption as it is usually locallized in the central part. The $\tilde{B}_\theta(m=2)$ in Fig.3 means the poloidal component of magnetic perturbation with poloidal mode number m=2. This precursor oscillation grows in stage 2 to form large magnetic islands. Figure 4 illustrates a tomographic reconstruction of contours of equal X-ray emissivity for m=2 mode.[8] In stage 3, the central electron temperature starts to decrease, indicating strong degradation of confinement of plasma. Some nonlinear phenomena occur in this stage which include nonlinear coupling of two modes with different helicities and the associated onset of stochasticity of magnetic field line. Finally in stage 4, the total toroidal current in plasma drops rapidly either to a lower level which will be recovered to a certain level (minor disruption), or to a total loss (major disruption). Figure 5 shows the observed X-ray intensity at the center in case of minor disruptions, where a seriers of minor disruptions is observed throughout the discharge. The partial disruption[9] is distinguished from the minor disruption by the fact that the central electron temperature is maintained and only the thermal energy of electrons in the middle radius region is transported to the periphery. This locally flattened profile

of electron temperature is recovered as is the case with the minor disruption.

B) Magnetohydrodynamic simulation

The general form of arbitrary linear perturbation $\delta f(r, \theta, \phi)$ assumes the form, $\delta f = \tilde{f}(r) \exp[\, i\,(m\theta - n\phi)\,]$, where θ and ϕ are poloidal and toroidal angles, and m and n are integers. The surface r=const. coincides with the magnetic surface. On the rational surface , $r=r_{m,n}$, where the rotational transform angle ι is equal to $2nn/m$, the gradient of arbitrary pertubation with mode numbers m and n is perpendicular to the equilibrium static magnetic field $\vec{B}_0$; $\vec{B}_0 \cdot \nabla\delta f(r,\theta,\phi) = 0$. It is familiar in the linear stability analysis of plasmas that unstable modes grow near the localized region about the rational surface. The rotational transform angle ι of the tokamak is a decreasing function of r, so that the radii of rational sufaces $r_{2,1}$, $r_{3,2}$ and $r_{1,1}$ satisfies the inequilities

$$r_{1,1} < r_{3,2} < r_{2,1} \quad . \tag{2.1}$$

The sawtooth oscillation grows in the inner part around the surface $r = r_{1,1}$. The observed oscillation with m=2 is thought to be a unstable tearing mode with m=2 and n=1, growing near the outer surface, $r=r_{2,1}$. At the radius $r=r_{3,2}$ inbetween, another unstable tearing mode with m=3, n=2 grows. The unstable magnetic pertubation with (m,n) grows to form m pieces of magnetic islands centered at the surface $r=r_{m,n}$. For instace, the islands located near the two surfaces $r_{3,2}$ and $r_{2,1}$ grow further until two islands originating from

different surfaces overlap, which results in the destruction of magnetic surface. In this case, the intersection points of a single field line through a poloidal surface ϕ=0, cover a finite area rather than lie on a single surface r=const., which means stochastic motion of r-coordinate of electrons sets in, because electrons tends to follow the magnetic field line. This enormous amount of radial electron transport is a central mechanism of disruption phenomena in tokamaks. A rather global mode coupling between the sawtooth oscillation and the tearing mode with m=2, and n=1 (2/1-mode in short) yields the major or minor disruption, while the fairly localized coupling between the 2/1- and 3/2-modes is responsible to the local disruptions.[9]

The basic system in our numerical simulation is a reduced set of resistive magnetohydrodynamic equations[10], which are in a cylindrical coodinate system (r,θ,z),

$$\frac{\partial}{\partial t} A + \overrightarrow{U_\perp} \cdot \nabla_\perp A = - \eta J + B_{oz} \frac{\partial}{\partial z} \Phi, \tag{2.2}$$

$$\frac{\partial}{\partial t} \Omega + \overrightarrow{U_\perp} \cdot \nabla_\perp \Omega = R_m (\overrightarrow{B_\perp} \cdot \nabla_\perp J + B_{oz} \frac{\partial}{\partial z} J), \tag{2.3}$$

$$\Omega = -\nabla_\perp^2 \Phi \quad , \tag{2.4}$$

$$J = -\nabla_\perp^2 A \quad . \tag{2.5}$$

Here the suffix $\perp$ means the (r, θ) plane, the constant B_{oz} the z-component of the unperturbed magnetic field $\vec{B}_o$, J the electric current in the z-direction, and A and Φ the z-

component of magnetic vector potential and the stream function respectively which are related to the magnetic field by

$$\vec{B} = \vec{B}_\perp + B_{oz}\,\hat{z} = \nabla_\perp A \times \hat{z} + B_{oz}\,\hat{z} \quad . \tag{2.6}$$

and to the flow velocity $\vec{U}_\perp$ by

$$\vec{U}_\perp = \nabla_\perp \Phi \times \hat{z} \quad , \tag{2.7}$$

where $\hat{z}$ is a unit vector in the z-direction. The two equations (2.4) and (2.5) represent the selfconsistency between J and A, and the vorticity Ω and Φ. This form of reduced MHD is obtained from the full MHD at the expense of rapid process of compressional Alfvèn mode, which is irrelevant to the disruption phenomena in tokamaks. The unperturbed plasma considered has a straight cylindrical form which contacts with a conducting wall at the radius a. To approximate the toroidal plasma by the cylindrical one, we assign a periodicity, $z=2\pi R_0$, in the z-direction. The important transport coefficient, the resistivity η, is assumed to keep a steady profile $\eta(r)$ satisfying $\eta(r)J_o(r)=$ =const. where the unperturbed current profile $J_o(r)$ is illustrated in Fig.6. The profile prescribed is unstable to both 2/1-and 3/2-tearing modes. The magnetic Reynolds number R_m defined by $(\tau_R/\tau_A)^2$ is 10^8, where two characteristic time scales are the Alfvèn transit time τ_A and the resistive time τ_R defined by $\tau_A=R_0(\mu_0\rho)^{\frac{1}{2}}/B_{z0}$ and $\tau_R = a^2\mu_o/\eta_o$. Numerical integration of the reduce MHD has been performed to investigate the evolution of the unstable state. In the initial linear stage, two independent unstable 2/1- and 3/2-

modes grow exponentially near each rational surface. The mode structures for the pertubed current $\delta J(r,\theta)$ at a time $t=1.0 \times 10^{-3}$ are depicted in Fig.7(a) for 2/1-mode, and Fig.7(b) for 3/2-mode. The time is scaled by the resistive time τ_R. In the intermediate stage at time $t = 2.7 \times 10^{-3}$, the structure of total current $J_o + \delta J$ is illustrated in Fig.8. The high current density region is deformed to the ellipse from the initial circle, according to the development of m=2 perturbation. Figure 9 shows the superposition of the points of intersection of 13 magnetic field lines, whose initial positions are marked with squares at the same time as in Fig.8. One can see in Fig.9 the deformation of unperturbed nested circular magnetic surfaces in the central and the periferal region, two large m=2 islands, three small m=3 islands and a chaotic magnetic layer around the separatrix of m=2 islands. The central high current region in Fig.8 coincides with the central regular region having the magnetic surface in Fig.9. In the large m=2 islands together with stochastic layer, the current density becomes low as shown in Fig.8. Appearance and growth of the stochastic area of the magnetic field line accelerate the nonlinear evolution of the spatial structure of the current $J(r,\theta)$. In the later stage at $t=3.25 \times 10^{-3}$, the stochastic region prevails almost whole area as shown in Fig.11, and corresponding contour of the total current becomes irregular as illusterated in Fig.10. The illuminating dynamics in the transient stage between $t=2.7 \times 10^{-3}$ and 3.25×10^{-3} will be reported elsewhere.

§3.Hamiltonian dynamical models of magnetic field line

Boozer[11] has proved that an arbitrary magnetic field $\vec{B}(\vec{r})$ satisfying $\mathrm{div}\vec{B} = 0$ can be written in a form

$$\vec{B} = \nabla\Psi \times \nabla\theta + \nabla\phi \times \nabla\Psi_p \quad . \tag{3.1}$$

If the magnetic field has toroidal symmetry as is the case with the unpertubed field $\vec{B}^{(0)}$ in tokamak, Ψ_p in Eq (3.1) is a function only of Ψ;

$$\Psi_p = \Psi_p{}^{(0)}(\psi) \quad . \tag{3.2}$$

The functions Ψ_p and ψ represent the poloidal and toroidal magnetic fluxes (see Fig.2). We may choose the angle variable ϕ as the true toroidal angle, while the angle θ becomes no longer a poloidal angle in a geometrical sense,but a generalized poloidal angle which depends on ψ indicating radial position and the true poloidal angle.[12]. The coordinates (ψ,θ,ϕ) are more convenient to treat the magnetic field line than the cartesian or cylindrical coordinates. A single magnetic field line can be described by two functions $\psi(\phi)$ and $\theta(\phi)$. The equations for $\psi(\phi)$ and $\theta(\phi)$ are

$$\frac{d\Psi}{d\phi} = \frac{\vec{B}\cdot\nabla\Psi}{\vec{B}\cdot\nabla\phi} = \frac{\nabla\phi\times\nabla\Psi_p\cdot\nabla\Psi}{\nabla\Psi\times\nabla\theta\cdot\nabla\phi}$$

$$= \frac{\nabla\Psi\times\nabla\phi\cdot\left[\nabla\Psi\dfrac{\partial\Psi_p}{\partial\Psi} + \nabla\theta\dfrac{\partial\Psi_p}{\partial\theta} + \nabla\phi\dfrac{\partial\Psi_p}{\partial\phi}\right]}{\nabla\Psi\times\nabla\theta\cdot\nabla\phi}$$

$$= -\frac{\partial}{\partial\theta}\Psi_p(\Psi,\theta,\phi) \tag{3.3}$$

and

$$\frac{d\theta}{d\phi} = \frac{\partial}{\partial\Psi}\Psi_p(\Psi,\theta,\phi) \quad . \tag{3.4}$$

Notice that the Eqs.(3.3) and (3.4) are identical to the Hamiltonian mechanics in form. The variables Ψ and θ are canonically conjugate action and angle variables, and Ψ_p and ϕ are Hamiltonian and the time variable. The general magnetic field line can be described by a time-dependent Hamiltonian with one spatial degree of freedom.

The perturbed field $\vec{B}^{(1)}$ due to some instabilities are now described by the Hamiltonian $\Psi_p\ (\Psi,\theta,\phi)$,

$$\Psi_p(\Psi,\theta,\phi) = \Psi_p^{(0)}(\Psi) + \sum_{m,n}\Psi_{m,n}(\Psi)\exp(im\theta - in\phi) + c.c. \quad , \tag{3.5}$$

where the summation is over integer values for m and n.

The points of intersection of a single field line through a poloidal surface is the Poincarè plot in phase space (Ψ,θ) every 2π period of "time variable" ϕ. The relation between one point $(\Psi_n,\ \theta_n)$ to the next one $(\Psi_{n+1},\theta_{n+1})$ is called the mapping. The simplest mapping derived from the unperturbed Hamiltonian $\Psi_p = \Psi_p^{(0)}(\Psi)$ is

$$\left.\begin{aligned} \Psi_{n+1} &= \Psi_n \quad , \\ \theta_{n+1} &= \theta_n + 2\pi\Psi_p^{(0)\prime}(\Psi_{n+1}) \quad , \end{aligned}\right\} \tag{3.6}$$

which is called the twist mapping. The quantity $2\pi\Psi_p^{(0)\prime}(\Psi_{n+1})$ is the rotational transform angle ι defined in §1. A generalized mapping in the perturbed case assumes the form

$$\Psi_{n+1} = \Psi_n + f(\Psi_{n+1}, \theta_n), \tag{3.7}$$

$$\theta_{n+1} = \theta_n + 2\pi\Psi_p^{(0)'}(\Psi_{n+1}) + g(\Psi_{n+1}, \theta_n), \tag{3.8}$$

where f and g are periodic in θ. As the Hamiltonian dynamics (3.3) and (3.4) are conservative, the mapping (3.7) and (3.8) must be area-preserving, so that the Jacobian should be unity;

$$\frac{\partial(\Psi_{n+1}, \theta_{n+1})}{\partial(\Psi_n, \theta_n)} = 1 \ . \tag{3.9}$$

A large class of mappings defined by (3.7) and (3.8) become area-preserving, as far as f and g satisfy

$$\frac{\partial}{\partial \Psi_{n+1}} f(\Psi_{n+1}, \theta_n) + \frac{\partial}{\partial \theta_n} g(\Psi_{n+1}, \theta_n) = 1 \ . \tag{3.10}$$

What is called the radial twist mapping is obtained by putting g=0 and f= Asinθ;

$$\Psi_{n+1} = \Psi_n + A \sin\theta_n \tag{3.11}$$

$$\theta_{n+1} = \theta_n + 2\pi \Psi_p^{(0)'}(\Psi_{n+1}) \quad . \tag{3.12}$$

Further if the rotational transform in Eq.(3.12) is a linear function of Ψ_{n+1};

$$2\pi \Psi_p^{(0)'}(\Psi_{n+1}) = 2\pi \Psi_p^{(0)'}(<\Psi>) + 2\pi \Psi_p^{(0)''}(<\Psi>)(\Psi_{n+1} - <\Psi>) \ , \tag{3.13}$$

putting the right-hand side of Eq.(3.13) to I_{n+1}, we have the famous standard mapping

$$I_{n+1} = I_n + K\sin\theta_n \tag{3.14}$$

$$\theta_{n+1} = \theta_n + I_{n+1} \tag{3.15}$$

and the nonlinearity parameter K is

$$K = 2\pi A \Psi_p^{(0)m}(<\Psi>) \quad . \tag{3.16}$$

The more realistic model is the continuous ϕ Hamiltonian system. A single perturbation with (m,n) in Eq.(3.5) does not cause stochasticity, and need another mode (m', n') for chaos. The helicity for two modes must be different; $m'/n' \neq m/n$. The two-wave Hamiltonian model thus obtained will be discussed in section 5 in detail.

We note that the standard mapping (3.14) and (3.15) are equivalent to the continuous ϕ Hamiltonian system described by the Hamiltonian,

$$H(I,\theta,\phi) = \frac{1}{2} I^2 + K \sum_{n=-\infty}^{\infty} \cos(\theta - n\phi) \quad . \tag{3.17}$$

§4. Radial twist mapping and long-time tail[4)]

The radial twist mapping [RTM] introduced in §3 to describe the toroidal magnetic field line is of the general form,

$$Y_{n+1} = Y_n + A\, f(X_n) , \tag{4.1}$$

$$X_{n+1} = X_n + \alpha(Y_{n+1}) . \tag{4.2}$$

The arbitrary function $\alpha(Y)$ means the rotation number of the angle variable $2\pi X$, the function $f(X)$ represents a periodic dynamic force satisfying the condition $f(X) = f(X+1)$, and A is a parameter. To iterate within a limited steps, it is sufficent to use the linearized version of the rotation number $\alpha(Y)$. If the force is sinusoidal, the standard mapping [SM],

$$Y_{n+1} = Y_n + A \sin 2\pi X_n , \tag{4.3}$$

$$X_{n+1} = X_n + Y_{n+1} , \tag{4.4}$$

is obtained from Eqs.(4.1) and (4.2) by linearization.

As far as the long-time prediction is concerned, however, SM does not approximate the more realistic radial twist mapping. This section cencerns a theory of long-time behavior of RTM, and show that the turbulent diffusion coefficient of Y variable decays as $t^{-1/2}$ to a quasilinear value. Exceptional case is SM, where the eventual value of diffusion coefficient is different from the quasilinear one.

Direct numerical iteration of the mapping has been performed to obtain the diffusion coefficiet D defined by

$$D = \lim_{N\to\infty} \frac{P_N}{2N} . \tag{4.5}$$

Here the mean square average P_N is

$$P_N = \langle (Y_N - Y_0)^2 \rangle, \tag{4.6}$$

where the brackets mean the average over the initial position X_0;

$$\langle F \rangle = \int_0^1 dX_0 F(X_0). \tag{4.7}$$

We find a striking contrast between the cases of SM and RTM. The diffusion coefficient of SM case is illustrated in Fig.12 Similar curves are obtained by Rechester and White[13], by Rechester, Rosenbluth and White [14] and by Meiss et al[15]. Results of RTM cases reveal a monotonic dependence on the parameter A as illustrated in Fig.13. It is to be noted that the diffusion coefficient is nearly equal to D_Q ($=A^2/4$) when A>1 either in Fig.13a) $a = Y^2/2$ or Fig.13 b) $a=(Y^2 - 1)/2$. The periodic force f is sinusoidal for both cases.

Our analytical study of the mean square average P_N starts with a functional integral representation,[16),13)]

$$P_N = \sum_{m_1=-\infty}^{\infty} \cdots \sum_{m_{N-1}=-\infty}^{\infty} \int_0^1 \cdots \int_0^1 dX_0 \cdots dX_{N-1} Y_N^2$$

$$exp\left[\sum_{j=1}^{N-1} 2\pi m_j i \left(X_j - X_{j-1} - a(Y_j) \right) \right] \tag{4.8}$$

where assuming the initial action Y_0 to be zero,

$$Y_j = A \sum_{p=0}^{j-1} f(X_p) \quad . \tag{4.9}$$

The m_j (j=1, $\cdots$, N-1) take on integer values. The main contribution to the integral (4.8) in the case of large A comes from the part obtained by putting all the m_j equal to zero;

$$P_N = P_Q = \int_0^1 \cdots \int_0^1 dX_0 \cdots dX_{N-1} Y_N^2 = \frac{A^2}{4} 2N \quad . \tag{4.10}$$

To obtain the last equality in Eq.(4.10), we have used the sinusoidal force for $f(X)$. The form P_Q is the result of the random-phase approximation or the quasilinear approximation. When A is larger than unity, the quasilinear value P_Q is dominant over the rest δP_N which comes from the terms with finite m_j. In fact, the deviation δP_N is negligible in the numerical curves in Figs.13(a) and (b), where the diffusion coefficient D is scaled by the quasilinear one $D_Q(=A^2/4)$. Nevertheless, δP_N is important, because it gives a new effect, the long-time tail, in the case of RTM and a finite contribution in the limitting case of SM. To estimate δP_N, we introduce the Fourier decompositions

$$e^{iq\alpha(Y)} = \int_{-\infty}^{\infty} dk\, \sigma(k,q)\, e^{ikY} \quad , \tag{4.11}$$

where $\sigma(k,q)$ becomes a delta-function in the case of SM;

$$\sigma(k,q) = \delta(k-q), \tag{4.12}$$

and, using sinusoidal force for $f(X)$,

$$e^{ip f(x)} = \sum_{m=-\infty}^{\infty} J_m(p)\, e^{2\pi i m X} \quad , \tag{4.13}$$

where $J_m(p)$ is the Bessel function. The conbinations of Eqs.(4.9),(4.11) and (4.13) yields a formula,

$$\exp\left[-2\pi m_j i\alpha(Y_j)\right]$$

$$= \left[\int_{-\infty}^{\infty} dk\sigma(k,-2\pi sgn(m_j)) \prod_{p=0}^{j-1} \sum_{m=-\infty}^{\infty} J_m(kA) e^{2\pi m i X_p}\right]^{|m_j|} \quad . \tag{4.14}$$

Three principal contributions $\delta P_N^{(i)}(i=1,2,3)$ to δP_N are as follows.

1) $m_j \neq 0$, $m_k = 0$ for $k \neq j$; $j=1,\cdots, N-1$

$$\delta P_N^{(1)} = \frac{A^2}{2}\int_{-\infty}^{\infty} dk\,[\sigma(k,-2\pi)+\sigma(k,2\pi)]\,J_0(kA)\,\frac{1-J_0^{N-1}(kA)}{1-J_0(kA)}$$
$$-\frac{A^2}{2}\int_{-\infty}^{\infty} dk\,[\sigma(k,-2\pi)+\sigma(k,2\pi)]\,J_2(kA)\,\frac{1-J_0^{N-1}(kA)}{1-J_0(kA)}$$
$$-\frac{A^2}{2}\int_{-\infty}^{\infty} dk\,[\sigma(k,-2\pi)+\sigma(k,2\pi)]\,2J_1^2(kA)\left[\frac{d}{dJ_0}\,\frac{J_0(X)-J_0^{N-1}(X)}{1-J_0(X)}\right]_{X=kA}$$
$$-\frac{A^2}{2}\int_{-\infty}^{\infty} dk\,[\sigma(k,-4\pi)+\sigma(k,4\pi)]\,J_2(kA)\,\frac{1-J_0^{N-1}(kA)}{1-J_0(kA)}. \qquad (4.15)$$

For the SM case, it becomes for large N

$$\lim_{N\to\infty}\delta P_N^{(1)} = A^2\,\frac{J_0(2\pi A)-J_2(2\pi A)}{1-J_0(2\pi A)} - \frac{2A^2J_1^2(2\pi A)}{[1-J_0(2\pi A)]^2} - A^2J_2(4\pi A)\,\frac{1}{1-J_0(4\pi A)}. \qquad (4.16)$$

2) m_j, $m_{j+1} \neq 0$, $m_i=0$ for $i\neq j$, $j+1$; $j=1,\cdots,N-2$

$$\delta P_N^{(2)} = -\frac{A^2}{2}\iint_{-\infty}^{\infty} dk_1\,dk_2\,[\sigma(k_1,-2\pi)\sigma(k_2,-2\pi)+\sigma(k_1,2\pi)\sigma(k_2,2\pi)]$$
$$\times J_0((k_1+k_2)A)\,J_0(k_2A)\,\frac{1-J_0^{N-1}((k_1+k_2)A)}{1-J_0((k_1+k_2)A)}$$
$$-\frac{A^2}{2}\iint_{-\infty}^{\infty} dk_1\,dk_2\,[\sigma(k_1,-2\pi)\sigma(k_2,2\pi)+\sigma(k_1,2\pi)\sigma(k_2,-2\pi)] \qquad (4.17)$$
$$\times J_0((k_1+k_2)A)\,J_2(k_2A)\,\frac{1-J_0^{N-1}((k_1+k_2)A)}{1-J_0((k_1+k_2)A)}$$
$$+\frac{A^2}{2}\iint_{-\infty}^{\infty} dk_1\,dk_2\,[\sigma(k_1,-2\pi)\sigma(k_2,-2\pi)+\sigma(k_1,2\pi)\sigma(k_2,2\pi)]$$
$$\times 2J_1^2((k_1+k_2)A)\,J_0(k_2A)\left[\frac{d}{dJ_0}\,\frac{J_0(x)-J_0^{N-1}(x)}{1-J_0(x)}\right]_{x=(k_1+k_2)A}.$$

For the SM case,

$$\delta P_N^{(2)} = -J_2(2\pi A)NA^2 + \cdots. \qquad (4.18)$$

3) m_j, $m_{j+2} \neq 0$, $m_k=0$ for $k\neq j$, $j+2$; $j=1,\cdots,N-3$

$$\delta P_N^{(3)} = -\frac{A^2}{2}\iint_{-\infty}^{\infty} dk_1 dk_2 \left[\sigma(k_1,-2\pi)\sigma(k_2,-2\pi)+\sigma(k_1,2\pi)\sigma(k_2,2\pi)\right]$$
$$\times J_0((k_1+k_2)A)J_1^2(k_2A)\frac{1-J_0^{N-1}((k_1+k_2)A)}{1-J_0((k_1+k_2)A)}$$
$$-\frac{A^2}{2}\iint_{-\infty}^{\infty} dk_1 dk_2 \left[\sigma(k_1,-2\pi)\sigma(k_2,2\pi)+\sigma(k_1,2\pi)\sigma(k_2,-2\pi)\right] \qquad (4.19)$$
$$\times J_0((k_1+k_2)A)J_1^2(k_2A)\frac{1-J_0^{N-1}((k_1+k_2)A)}{1-J_0((k_1+k_2)A)}.$$

For the SM case,

$$\delta P_N^{(3)} = -J_1^2(2nA)NA^2 + \cdots . \qquad (4.20)$$

To obtain an asymptotic form of δP_N for large N, it is necessary to investigate the integral

$$\int_{-\infty}^{\infty} dk\, F_1(k)\frac{1-J_0^{N-1}(kA)}{1-J_0(kA)} , \qquad (4.21)$$

where the $F_1(k)$ is an arbitrary function.

As the integrand in Eq.(4.21) contributes to the integral only from small value of kA, with use of the expansion $J_0(x) = 1-x^2/4 + \cdots$, Eq.(4.21) becomes

$$\int dk\, F_1 \frac{1-J_0^{N-1}}{1-J_0} \sim 2F_1(0)\int_0^{k_0} dk\, \frac{1-[1-\frac{(kA)^2}{4}]^N}{(kA)^2/4} . \qquad (4.22)$$

where k_0 is arbitray finite constant satisfying $k_0A \leq 1$.

Changing the variable of integration from k to y by the substitution $y=kA\sqrt{N}/2$, we have

$$\int dk\, F_1 \frac{1-J_0^{N-1}}{1-J_0} \sim \frac{4F_1(0)\sqrt{N}}{A}\int_0^{\infty} dy\, \frac{1-e^{-y^2}}{y^2} = 4\sqrt{\pi}F_1(0)\sqrt{N}/A . \qquad (4.23)$$

We obtain similarly an asymptotic form of another integral in Eq.(4.15) and (4.17);

$$\int_{-\infty}^{\infty} dk\, F_2(k)\, 2J_1^2(kA) \left[\frac{d}{dJ_0} \frac{J_0(X) - J_0^{N-1}(X)}{1 - J_0(X)} \right]_{X=kA} \sim 4\sqrt{\pi} F_2(0) \sqrt{N}/A . \qquad (4.24)$$

Thus the total δP_N has the asymtotic forms for RTM

$$\delta P_N = \sum_{i=1}^{3} \delta P_N^{(i)} = \sqrt{N} A \sum_{i=1}^{3} \alpha^{(i)} , \qquad (4.25)$$

where

$$\alpha^{(1)} = 0, \qquad (4.26)$$

$$\begin{aligned} \alpha^{(2)} = & -2\sqrt{\pi} \int_{-\infty}^{\infty} dy \left[\sigma(y, -2\pi)\sigma(-y, -2\pi) + \sigma(y, 2\pi)\sigma(-y, 2\pi) \right] J_0(yA) \\ & -2\sqrt{\pi} \int_{-\infty}^{\infty} dy \left[\sigma(y, -2\pi)\sigma(-y, 2\pi) + \sigma(y, 2\pi)\sigma(-y, -2\pi) \right] J_2(yA) \\ & +2\sqrt{\pi} \int_{-\infty}^{\infty} dy \left[\sigma(y, -2\pi)\sigma(-y, -2\pi) + \sigma(y, 2\pi)\sigma(-y, 2\pi) \right] J_0(yA), \end{aligned} \qquad (4.27)$$

$$\alpha^{(3)} = -2\sqrt{\pi} \int_{-\infty}^{\infty} dy \left[\sigma(y, 2\pi) + \sigma(y, -2\pi) \right] \left[\sigma(-y, 2\pi) + \sigma(-y, -2\pi) \right] J_1^2(yA), \qquad (4.28)$$

and for SM,

$$\delta P_N = -NA^2 \left[J_2(kA) + J_1^2(kA) \right] . \qquad (4.29)$$

Final expression for the diffusion coeffifcient is

$$D = \lim_{N \to \infty} \frac{P_N}{2N} = \lim_{N \to \infty} \frac{P_Q + \delta P_N}{2N} = \frac{A^2}{4} + \delta D \qquad (4.30)$$

with

$$\delta D = \begin{cases} \lim_{N\to\infty} O\left(\frac{1}{\sqrt{N}}\right) = 0 \quad , & (RTM) \\ -[J_2(2\pi A) + J_1^2(2\pi A)]A^2/2 \quad , & (SM) \end{cases} \tag{4.31}$$

which agrees well with the numerical results.

The fact that the mean square value of Y increases with time as $\sqrt{N}$ suggests the existence of long-time tail for the autocorrelation function of acceleration $\dot{Y}$. Discussion on this will come again in §6.

The SM gives a good approximation to RTM as for the short-time behaviour is concerned. To discuss the adequacy of representing the RTM with the SM, we estimate the critical time N_c, beyond which the prediction of the RTM differs from that of the SM. The main contribution to δP_N comes from the second integral in Eq.(4.19), so δD is given by

$$\delta D \propto \begin{cases} -\lim_{N\to\infty} \left(\frac{gA}{\sqrt{N}}\right) = 0 \quad , & (RTM) \\ -\frac{1}{4} J_2(2\pi A)\, A^2 \quad , & (SM) \end{cases} \tag{4.32}$$

where the factor g is given by

$$g = \sqrt{\pi} \int_{-\infty}^{\infty} dk_2 J_2(k_2 A) \left[\sigma(-k_2, -2\pi) \times \sigma(k_2, 2\pi) + \sigma(-k_2, 2\pi)\sigma(k_2, -2\pi)\right]. \tag{4.33}$$

We can now estimate the critical time N_c by setting $gA/\sqrt{N}$ in Eq. (4.32) equal to the value of δD in SM case to obtain

$$N_c = [2g/J_2(2\pi A)A]^2. \tag{4.34}$$

The value of N_c is sensitive to the rotation number $\alpha(Y)$. In particular when $\alpha = Y^2/2$, g is given by $g \approx n^{-3/2}$.

§5. Chaotic orbits in the two-wave Hamiltonian model and decay of correlation function with the power law [5)]

If the Hamiltonian (3.5) retains two modes with different sets of (m,n), it is called the two-wave Hamiltonian. After a transformation of variables, the paradigm form of two-wave Hamiltonian is obtained as

$$H = \tfrac{1}{2}v^2 - M\cos x - P\cos[k(x-t)] \quad , \qquad (5.1)$$

where k,M,P are parameters and k is assumed to be rational; $k=r/p$. We find a recursion relation for the autocorrelation function for chaotic orbit and its decay with the power law[5)], from the selfsimilar nature[17)] of the two-wave Hamiltonian found by Escande and Doveil.[18)] They have developed a renormalization transforma'ion which blows up a special region of phase space structure in the neighbourhood of a certain orbit. The orbit is dominantly influenced by two adjacent resonant structures in phase space which exist both upper and lower sides of the orbit. The orbit is described well by the new two-wave Hamiltonian.

$$H' = \tfrac{1}{2}v'^2 - M'\cos x' - P'\cos[k'(x' - t')] \quad , \qquad (5.2)$$

which has the same form as Eq.(5.1) although variables x',v', t' and parameters M',P',k', are transformed from original variables and parameters through a renomalization transformation.

The chaotic orbit we consider belongs to denumerable set of orbits whose mean velocity $\langle v \rangle$ is given by

$$\langle v \rangle = \frac{k}{k + z_m - 1} \qquad (5.3)$$

with the zoning number z_m given by

$$z_m = \tfrac{1}{2}[\, m + \sqrt{m^2 + 4}\,] \quad , m = 1, 2, \cdots \quad . \quad (5.4)$$

Specifically if m=1, z_m becomes the golden mean $z_1=[1+\sqrt{5}]/2$. These values of zoning number z_m are invariant through the renomalization transformation, which however transform $\langle v\rangle$, k, M and P to new values $\langle v'\rangle$, k', M', P'. After a sequence of transformation, $\langle v\rangle_n$ and k_n converge to respective values

$$\langle v\rangle_n \rightarrow \langle v\rangle_*,$$

$$k_n \rightarrow k_*. \quad (5.5)$$

Sequence (M_n, P_n) has a non-trivial evolution. The mapping has a single hyperbolic fixed point (M_*, P_*) with stable (S) and unstable (U) manifolds as shown in Fig.14.

The autocorrelation function of velocity is defined by the ensemble average,

$$C_{vv}^{A}(s) \equiv \langle \delta v_t \, \delta v_{t+s} \rangle = (1/\Gamma) \int_D d\mathbb{X} \, \delta v_t(\mathbb{X}) \delta v_{t+s}(\mathbb{X}), \quad (5.6)$$

with

$$\delta v_t(\mathbb{X}) = v_t(\mathbb{X}) - \langle v_t \rangle \quad (5.7)$$

Here $v_t(\mathbb{X})$ means the velocity at time t with an initial position $\mathbb{X}$ in phase space, and Γ is the volume of the phase space D which the individual orbit covers and where the integration in Eq.(5.6) is overtaken. We find a recursion equation for the correlation function in ω-space defined by

$$C_{vv}^{A}(\omega) = \int_0^\infty ds\, e^{i\omega s} C_{vv}^{A}(s) \; . \quad (5.8)$$

After the n-th renormalization transformation, we obtain the equation

$$C^{A}_{vv}(\omega;k,M.P) = \overline{\beta_n}\, C^{A}_{vv}(\overline{\alpha_n}\,\omega, k_n, M_n, P_n) \tag{5.9}$$

where

$$\overline{\alpha_n} = \alpha_1\alpha_2\cdots\alpha_n\,, \qquad \overline{\beta_n} = \beta_1\beta_2\cdots\beta_n\,. \tag{5.10}$$

The mean velocity <v> is a function of k, so we have suppressed it. For the explicit form for α_i and also derivation of the scaling relation (5.9), the readers should refer to the Ref.5.

The following analysis to derive the decay of correlation with the power law is only applicable to the neighbourhood of the critical Hamiltonian H_* with invariant parameters (k_*, M_*, P_*) under the renormalization transformation. Consider a tangent mapping about the fixed point;

$$\Delta X_{n+1} = L_* \Delta X_n\,, \tag{5.11}$$

where

$$\Delta X_n = (\Delta \ln M_n, \Delta \ln P_n, \Delta k_n) = \left(\frac{(M_n - M_*)}{M_*}, \frac{P_n - P_*}{P_*}, k_n - k_*\right). \tag{5.12}$$

We do not need the explicit form of matrix L_*. Let the eigen values and eigen vectors of the matrix L_* be $\mu_\pm$, μ_k, and $\vec{w}_\pm$, $\vec{w}_k$;

$$L_* w = \mu w\,. \tag{5.13}$$

Only a single unstable eigen value μ_+ is larger than unity, while for the stable ones, $|\mu_-|$, $|\mu_k|< 1$.

The stable eigen vector $\vec{w}_-$ is given by

$$w_-=(1, -\xi^{-1}, 0) \ , \tag{5.14}$$

which suggests that the stable manifold S in Fig.14 is described by the equation

$$S(M, P, k)=MP^{\xi}-R(k)=0 \ , \tag{5.15}$$

where ξ is a universal constant.

Forms for $\ell n\alpha_n$, $\ell n\beta_n$ and $S(M_n, P_n, k_n)$ about the fixed point are required for later use. Since the eigen vector $\vec{w}_\pm$ has no components in the direction of $\vec{w}_k$, we have

$$k_n-k_*=\mu_k{}^n(k-k_*) \ . \tag{5.16}$$

As α_n and β_n in Eq.(5.10) are $\alpha(k_n)$ and $\beta(k_n)$, Taylor expanding them around k_* and using a short-hand notation $\alpha_* = \alpha(k_*)$, we have

$$\ln \alpha_n=\ln \alpha_*+\frac{d\ln\alpha_*}{dk_*}\mu_k{}^n(k-k_*) \ , \tag{5.17}$$

$$\ln \beta_n = \ln \beta_* + \frac{d \ln \beta_*}{dk_*} \mu_+^n (k - k_*) \ , \tag{5.18}$$

and $S_n \equiv S(M_n, P_n, h_n) = (\vec{s_*} \cdot \vec{\Delta X_n}) \quad ,$ (5.19)

where the vector $\vec{s_*}$ is defined by

$$s_* = \left(\frac{\partial S}{\partial \ln M_*}, \frac{\partial S}{\partial \ln P_*}, \frac{\partial S}{\partial k_*} \right), \tag{5.20}$$

which is normal to $\vec{w_-}$ and $\vec{w_k}$;

$$(s_* \cdot w_-) = (s_* \cdot w_k) = 0 \, . \tag{5.21}$$

An iterative use of Eq.(5.11) gives

$$\vec{\Delta X_n} = L_*^n \, \vec{\Delta X} \, , \tag{5.22}$$

where $\vec{\Delta X}$ can be decomposed as follows,

$$\begin{aligned} \vec{\Delta X} &= \left(\frac{M - M_*}{M_*}, \frac{P - P_*}{P_*}, k - k_* \right) \\ &= \Delta X_+ \, \vec{w_+} + \Delta X_- \, \vec{w_-} + \Delta k \, \vec{w_k} \ . \end{aligned} \tag{5.23}$$

Plugging Eq.(5.22) and (5.23) into Eq. (5.19) and using the orthogonality (5.21), we have

$$S_n = \Delta X_+ (s^* \cdot w_+) \mu_+^n . \tag{5.24}$$

A solution for the recursion equation (5.9) is

$$C_{vv}^{\Lambda}(\omega, k, M, P) = C_\beta(M, P, k) \left(\frac{\omega}{C_\alpha(M, P, k)} \right)^{-\delta}, \tag{5.25}$$

with

$$C_\alpha = S(M, P, k)^\mu , \tag{5.26}$$

$$C_\beta = S(M, P, k)^\nu . \tag{5.27}$$

The exponents μ, ν and δ are universal constants given by

$$\mu = \frac{\ln \alpha_*}{\ln \mu_+}, \tag{5.28}$$

$$\nu = -\frac{\ln \beta_*}{\ln \mu_+}, \tag{5.29}$$

$$\delta = \frac{d \ln \beta_*}{d \ln \alpha_*} . \tag{5.30}$$

Thus we have proved that the velocity time-correlation function decay with power law as $t^{-(1-\delta)}$.

§6. Fractional Brownian motion and long-time tail of magnetic field lines

We have performed numerical integration of the two-wave Hamiltonian system (5.1) and observed a correlation function of a particle velocity $v_t(\mathfrak{X})$ defined by the time average

$$C^T_{vv}(s) = \overline{\delta v_{t+s}(\mathfrak{X})\,\delta v_t(\mathfrak{X})}$$

$$= \frac{1}{T}\int_0^T dt\, \delta v_{t+s}(\mathfrak{X})\,\delta v_t(\mathfrak{X}) \quad , \tag{6.1}$$

with

$$\delta v_t(\mathfrak{X}) = v_t(\mathfrak{X}) - \overline{v_t(\mathfrak{X})} \quad , \tag{6.2}$$

where the time interval T is $2\pi\cdot 10^5$, sufficiently large as compared with the wave period $2\pi/k$. The time step Δt of the predictor-corrector method is $\pi/300$. Figure 15 shows the results for the conditions: M=0.04, P = 10^{-4}, k=16 and the initial position (x,v) = (0, 1.0). Plots in phase space at every 2π intervals are illustrated in Fig.15(a). The width Δv of the chaotic layer is less than the mean velocity $\bar{v}$, which situation matches the assumption made in the previous section. In Fig.15(b), the total velocity correlation $C^T_{vv}(s) + \bar{v}^2$ is plotted, and just the correlation $C^T_{vv}(s)$ in Fig.15(c). The same correlation $C^T_{vv}(s)$ vs. s is displayed in Figs.15(d) and (e) in the semi-logarithmic and logarithmic scales, respectively. Figure 15(e) shows clearly linearity of the curve, implying the decay with the power law. By fitting a

formula $C^{T}_{vv}(s) \propto s^{-\sigma}$ to the curve, we obtain a value of the exponent, $\sigma=0.22$.

Calculation of the power spectrum of velocity is accomplished to confirm the power law decay of velocity correlation function. The definition of the power spectrum is given by

$$I(\omega) = \frac{1}{2\pi} \int_0^{T'} d\tau \, |\delta v(\omega, \tau)|^2 \quad , \tag{6.3}$$

with

$$\delta v(\omega, \tau) = \frac{1}{T'} \int_{\tau}^{\tau+T'} dt \, \delta v_t \, e^{i\omega t} \quad , \tag{6.4}$$

where the dependence of δv_t on the initial position $\mathbf{x}$ is suppressed. The time interval T' has to be much larger than the characteristic time scale $2\pi/\omega$. It is straightforward to obtain a formula

$$I(\omega) = \frac{1}{\pi} Re \int_0^{\infty} ds \, C^{T}_{vv}(s) \, e^{i\omega s} \quad , \tag{6.5}$$

in the limit, $T' \to \infty$. In the present run. T' is chosen to be 4.12×10^5. Figure 16 shows $I(\omega)$ obtained under the same condition as in Fig.15. In the low-frequency range $\omega<1$, we can observe a turbulent spectrum as $\omega^{-\delta}$ with $\delta = 0.86$. The observed δ which is nearly equal to $1-\sigma$ is consistent with the formula (6.5) and that $C^{T}_{vv}(s)$ is proportional to $s^{-\sigma}$.

The statistical property of the coordinate x(t) is investigated under the same condition as in Figs.15 and 16. Figure 17(a) shows the time history of the deviation ξ defined by

$$\xi(t) = x(t) - \bar{v}t \quad . \tag{6.6}$$

We observe the variance $\sigma_{\xi\xi}(t)$ defined by

$$\sigma_{\xi\xi}(t) = \frac{1}{T}\int_0^T d\ell \left\{\xi(t+\ell) - \xi(\ell)\right\}^2 \quad . \tag{6.7}$$

The curves shown in Figs.17(b) and (c) are $\sigma_{\xi\xi}(t)$ vs.t in the semilogarithmic and logarithmic scales,respectively. Figure 17(c) indicates that the variance grows as t^{ν}. It is interesting that the power ν is observed to be $\nu = 1.7$. The present observation gives $\nu + \sigma = 1.92$, though the sum of the exponents should be precisely two. Note that the stochastic process $\xi(t)$ is able to be described by the fractional Brownian motion with persistence ($\nu > 1$), which is the diffusion-like motion "faster" than the ideal Brownian motion ($\nu = 1$) and "slower" than the straight orbit with constant velocity ($\nu = 2$). This characteristic feature of the stochastic orbit is illustrated clearly in Figure 17(a), where the orbit consists of the combination of intermittent straight motion and the ideal Brownian motion.

In order to discuss the long-time tail of the magnetic field line, we introduce next the Liouville equation for the distribution function $f(\psi,\theta,\phi)$ of the field line. the variables ψ,θ, and ϕ have been introduced already in §3. The distribution f is proportional to numbers of field line in a volume element $d\psi d\theta$. We may interpret f as a distribution function of electrons, if they follow precisely the magnetic field lines with a constant velocity. In this version, the variable ϕ should mean the real time variable. The evolution equation for f is

$$\frac{\partial}{\partial\phi} f = L(\phi) f \quad , \tag{6.8}$$

with

$$L(\phi) = -\frac{\partial H}{\partial \Psi}\frac{\partial}{\partial \theta} + \frac{\partial H}{\partial \theta}\frac{\partial}{\partial \Psi}. \tag{6.9}$$

Define a reduced distribution $g(\Psi,\phi)$ by

$$g(\Psi,\phi) = Pf \quad , \tag{6.10}$$

where the projection operator P is

$$Pf = \frac{1}{2\pi}\int_0^{2\pi} d\theta\, f(\Psi,\theta,\phi) \quad . \tag{6.11}$$

According to the reduction procedure due to the projection operator method, we obtain a formal transport equation in the from,

$$\frac{\partial}{\partial \phi} g(\Psi,\phi) = \frac{\partial}{\partial \Psi}\int_0^{\phi} d\phi' \hat{K}(\phi,\phi')\frac{\partial}{\partial \Psi} g(\Psi,\phi') \quad . \tag{6.12}$$

The memory kernel $\hat{K}$ is

$$\hat{K}(\phi,\phi') = P\left[\frac{\partial H}{\partial \theta}(\phi)\frac{\partial H}{\partial \theta}(\phi')\right] + O\left(\frac{\partial}{\partial \Psi}\right). \tag{6.13}$$

Thus to the order of second derivative with respect to Ψ, the transport equation (6.12) becomes the Fokker-Plack type with the diffusion coefficient,

$$D(\phi) = 2\int_0^{\phi} K(\tau)\, d\tau \quad . \tag{6.14}$$

and the memory kernel $K(\tau)$ is

$$K(\phi - \phi') = P\left[\frac{\partial H}{\partial \theta}(\phi)\frac{\partial H}{\partial \theta}(\phi')\right] \quad , \tag{6.15}$$

which is the autocorrelation function of the acceleration $\partial H/\partial\theta = -\dot{\Psi}$. It is shown in §4 that the diffusion coefficient $D(\phi)$ decays with the power law $\phi^{-1/2}$ to a finite value D_Q. This means that the correlation function $K(\tau)$ should have the form

$$K(\tau) = \frac{1}{2} D_Q \Gamma \exp(-\Gamma\tau) + O(\tau^{-3/2}) \quad , \tag{6.16}$$

that is a sum of exponentially decaying term and the long-time tail decaying with the power law $\tau^{-3/2}$.

A solution of the non-Markoffian transport equation (6.12) together with the kernel (6.15) is given by

$$g(\Psi,\phi) = \sum_k exp\left\{[-i\Omega(k)-\gamma(k)]\phi\right\} exp(ik\phi). \quad . \tag{6.17}$$

The complex frequency $\omega(k) = \Omega(k) + i\gamma(k)$ satisfies the dispersion relation

$$-i\omega(k) = -k^2 \int_0^\infty d\tau K(\tau) e^{i\omega(k)\tau} . \tag{6.18}$$

If the correletion function $K(\tau)$ has only the first term in Eq.(6.16) and $\Gamma >> k^2 D_Q$, the frequency $\omega(k)$ becomes $\omega(k) = -ik^2 D_Q/2$, which is the normal diffusion process. But when there exists a long-time tail in the correlation function, the real frequency $\Omega(k)$ is not negligible, so that the solution (6.17) propagates like the wave.

We show finally a numerical result which suggests the existence of long-time tail for correlation function of dv/dt even in the two-wave Hamiltonian system. Figure 18 shows the time evolution of the variance of velocity defined by

$$\sigma(t) = \frac{1}{T}\int_0^T ds[v_{t+s} - v_s]^2 . \tag{6.19}$$

If the present stochastic process were governed by the ideal diffution process with diffusion coefficient D, then the variance $\sigma(t)$ should grow simply as shown by the dotted line in Fig.18, the analytic form of which is given by

$$\sigma(t) = \frac{2}{3}u^2\left\{1 - \frac{96}{\pi^4}\sum_{n=0}^{\infty}\frac{1}{(2n+1)^4} exp[-\frac{\pi^2}{u^2}(n+\frac{1}{2})^2 Dt]\right\}, \tag{6.20}$$

where the $2u^2/3$ is the saturation value of $\sigma(t)$. The numerical curve however is oscillatory, suggesting the effect of long-time tail or the real frequency $\Omega(k)$ in the dispersion

relation (6.18). The explict analytic form for the numerical curve may assume the form

$$\sigma(t) = \frac{2}{3}u^2\left\{1 - \frac{96}{\pi^4}\sum_{n=0}^{\infty}\frac{1}{(2n+1)^4}\exp\left[-\frac{\pi^2}{u^2}(n+\frac{1}{2})^2 Dt\right]\cos(\Omega_n t)\right\}. \qquad (6.21)$$

§7 Summary and discussion

This article has attempted to show that the onset of chaos of the magnetic field line has a great influence on the subsequent rapid MHD evolution of plasmas resulting in the turbulence. Two unstable modes in toroidal plasmas grow linearly and couple nonlinearly to yield chaotic braided magnetic field lines, until there occurs a rapid quench of energy stored in the plasma and a disruption of plasma current. The magnetic chaos is a typical example in the Hamiltonion system which is connected to the macroscopic rapid phenomena. We have emphasized the fractional Brownian motion and the long-time tail, which originate from the selfsimilar structure in phase space for chaotic magnetic field lines.

The current disruption in tokamaks has been thought to be a magnetic relaxation phenomenon, in which an unstable equilibrium state relaxes into a new equilibrium state with the lower free-energy. In ideal MHD, all field line connection must be conserved ; the magnetic helicity defined as,

$$K_1 = \int_1 \vec{A}\cdot\vec{B}\,d^3x, \quad \nabla\times\vec{A}=\vec{B}, \tag{7.1}$$

is conserved, where the integral is over a flux tube for a single field line. The total energy (the magnetic, kinetic and internal energies) is another invariant in case of nondissipative MHD. As the kinetic and internal energies are negligibly small in tokamaks as compared with the magnetic one, the volume integral of magnetic energy defined as

$$W = \int_{tot} \frac{1}{2} B^2 d^3x \ , \tag{7.2}$$

must be conserved, where the integral is over the total plasma volume bounded by a conductive wall. In dissipative MHD, however, since the decay rate of K_1 is much less than that of W, Woltjer[19] first proved that the unstable plasma relaxes to a force-free state ($\vec{J} \times \vec{B} = 0$) with $\vec{J} = \mu_1 \vec{B}$, which is a minimum magnetic energy state subject to constraints K_1 = const. for each flux tube. The constants μ_1 are different in general for different field lines. The magnetic helicitities K_1 for braided field lines are mixed up through the magnetic chaos and the associated reconnection, so that the proper constant μ_1 for each field line becomes to take the same value μ. Taylor[20] introduced a weaker constraint,

$$K_{tot} = \int_{tot} \vec{A} \cdot \vec{B} d^3x = const. , \tag{7.3}$$

and conjectured that a global force-free current, $\vec{J} = \mu \vec{B}$, exists in a relaxed state, what is called the Taylor state. The Taylor state in tokamaks is a state with a spatially flattened toroidal current profile, touching the conductive wall at a finite value of current density and leading to a current disruption.

In conclusion, the detailed mechanisms of transport process connecting the initial unstable peaked current profile as shown in Fig.8 and the final flat current density, are left for future studies.

References

1) B.V.Chirikov, Phys.Rep. 52 (1979), 263.

2) H. Irie, J. Phys. Soc. Jpn. 54 (1985), 2883.

3) Y.H. Ichikawa, T. Kamimura and T. Hatori, Physica 29D(1987), 247.

4) T.Hatori, T.Kamimura and Y.H.Ichikawa, Physica 14D (1985), 193.

5) T.Hatori and H.Irie, Prog.Theor. Phys. 78 (1987), 249.

6) B.Carreras, H.R.Hicks, J.A.Holmes, and B.V.Waddell, Phys. Fluids 23 (1980), 1811.

7) J.A.Wesson, A.Sykes and M.F.Turner, Nucl.Fusion Supplement, Plasma Physics and Nuclear Fusion Research (IAEA,Vienna,1984) Vol.2, p.23, CN-44/E-I-3.

8) N.R.Sauthoff, S.Von Goeler and W.Stodiek, Nucl.Fusion 18 (1978), 1445.

9) S.Tsuji, Y.Nagayama, K.Miyamoto, Nucl.Fusion 25 (1985), 305.

10) H.R.Strauss, Phys. Fluids 19 (1976), 134.

11) A.H.Boozer, Phys. Fluids 26 (1983), 1288.

12) J.R.Cary and R.G.Littlejohn, Annals of Phys. 151 (1983), 1.

13) A.B.Rechester and R.B.White, Phys. Rev.Letters 44 (1980), 1586.

14) A.B.Rechester, M.N.Rosenbluth and R.B.White, Phys. Rev.A23 (1981), 2664.

15) J.D.Meiss, J.R.Cary, C.Grebogi, J.D.Crawford and A.N.Kaufman, Physica 6D (1983), 375.

16) B.Jouvet and R.Phythian, Phys.Rev. A19 (1979), 1350.

17) D.F.Eskande, Phys.Rep. 121 (1985), 165.

18) D.F.Eskande and F.Doveil, J.St. Phys. 26 (1981), 257.

19) L.Woltjer, Proc.Natl.Acad.Sci. USA 44 (1958), 489.

20) J.B.Taylor, Phys.Rev. Lett. 33 (1974), 1139.

Figure captions

Fig.1. Typical motion of a charged particle in a mirror geometry has three charateristic frequencies, the highest cyclotron frequency ω_c, the intermediate bounce frequency ω_b and the lowest drift frequency ω_d.

Fig.2. The tokamak configuration (a), and a typical magnetic field line and a magnetic surface (b).

Fig.3. Standard sequence of Tokamak disruption shows total current, magnetic oscillation and soft X-ray emission. The traces shown occupy 30msec.

Fig.4. Tomographic reconstruction of contours of equal X-ray emissivity for the m=2 mode.

Fig.5. Central line-integrated X-ray emissivity for a series of minor disruptions in a Tokamak.

Fig.6. Contours of the unperturbed toroidal current density (a) and its profile (b). Coordinates are scaled by the plasma radius, a.

Fig.7. Spatial structure of perturbed current density due to the tearing modes at time $1.0 \cdot 10^{-3}$. Fig.7 a) shows contours of equal positive (solid) and negative (dotted) current densities of an unstable 2/1-mode with m=2, n=1 growing near the radius $r_{2,1}$, and b) of another weakly unstable 3/2-mode with m=3, n=2 at the inner radius $r_{3,2}$. The maximum value of 2/1-mode is 6.3 times larger than that of 3/2-mode.

Fig.8. Contours of equal total current density, the unperturbed plus the perturbed current, observed at time $2.7 \cdot 10^{-3}$, showing central peak and two islands on both sides. The solid lines indicate negative current

and the dotted lines positive (note that the unperturbed current is negative).

Fig.9. Poincare plots at $t=2.7\cdot10^{-3}$ of several magnetic field lines, initial positions of which are marked by squares. There appears a chaotic region near the separatrix of major magnetic islands.

Fig.10. Contours of equal total current density, the unperturbed plus perturbed current, observed at time $3.25\cdot10^{-3}$ showing irregular pattern. The solid lines indicate negative current and the dotted lines positive (note that the unperturbed current is negative).

Fig.11. Poincare plots at $t=3.25\cdot10^{-3}$ of several field lines, initial positions of which are marked by squares. The chaotic region prevails in the whole area, except for the peripheral and central parts.

Fig.12. The diffusion coefficient scaled by D_Q $(=A^2/4)$ vs. A for the standard mapping.

Fig.13. The diffusion coefficient scaled by D_Q $(=A^2/4)$ vs. A for the radial twist mapping with a) $\alpha(Y) = Y^2/2$ and b) $\alpha(Y) = (Y^2-1)/2$.

Fig.14. The flow of renormalization transformation in (M,P) space. The line S described by the equation, $MP^{\zeta} = R(k_*)$, separates the chaotic region (upper) from the integrable one (lower).

Fig.15. The velocity autocorrelation function for parameters, M=0.04, $P=10^{-3}$, k=16 and the initial condition (x,v)=(0,1). a) Phase space plots at every 2π step. The total velocity correlation function, $c^T_{vv}(s) + v^2$

in (b) and the pure correlation $c^{T}_{vv}(s)$ in the c) linear, d) semilogarithmic and e) logarithmic scales.

Fig.16. The velocity power spectrum $I(\omega)$ obtained under the condition, $M=0.04$, $P=10^{-3}$, $k=16$ and $(x,v)=(0,1)$for an initial point, in the a) linear, b) semilogarithmic and c) logarithmic scales. The gradient of the solid line in c) shows the numerically obtained gradient of the averaged spectrum.

Fig.17. The time history (a) of the deviation $\xi(t)$ and the variance $\sigma_{\xi\xi}(t)$ vs. t in the b) semilogarithmic and c) logarithimic scales.

Fig.18. Time evolution of variance of velocity for a gloval chaotic orbit in the two-wave Hamiltonian system, under the condition $M=0.2$, $P=0.2$, $k=1.0$ and $(x,v) = (0, 0.6)$ for the initial position. The variance should grow along the dotted line, if the stochastic process were of the pure diffusion.

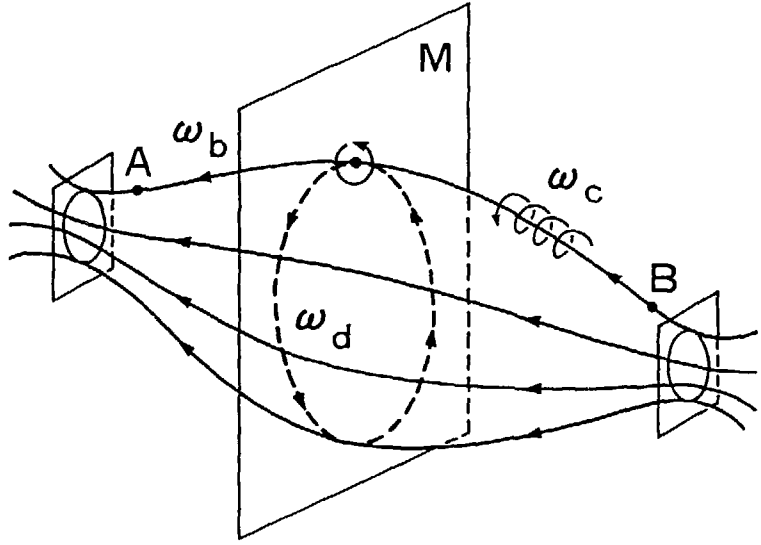

Fig. 1

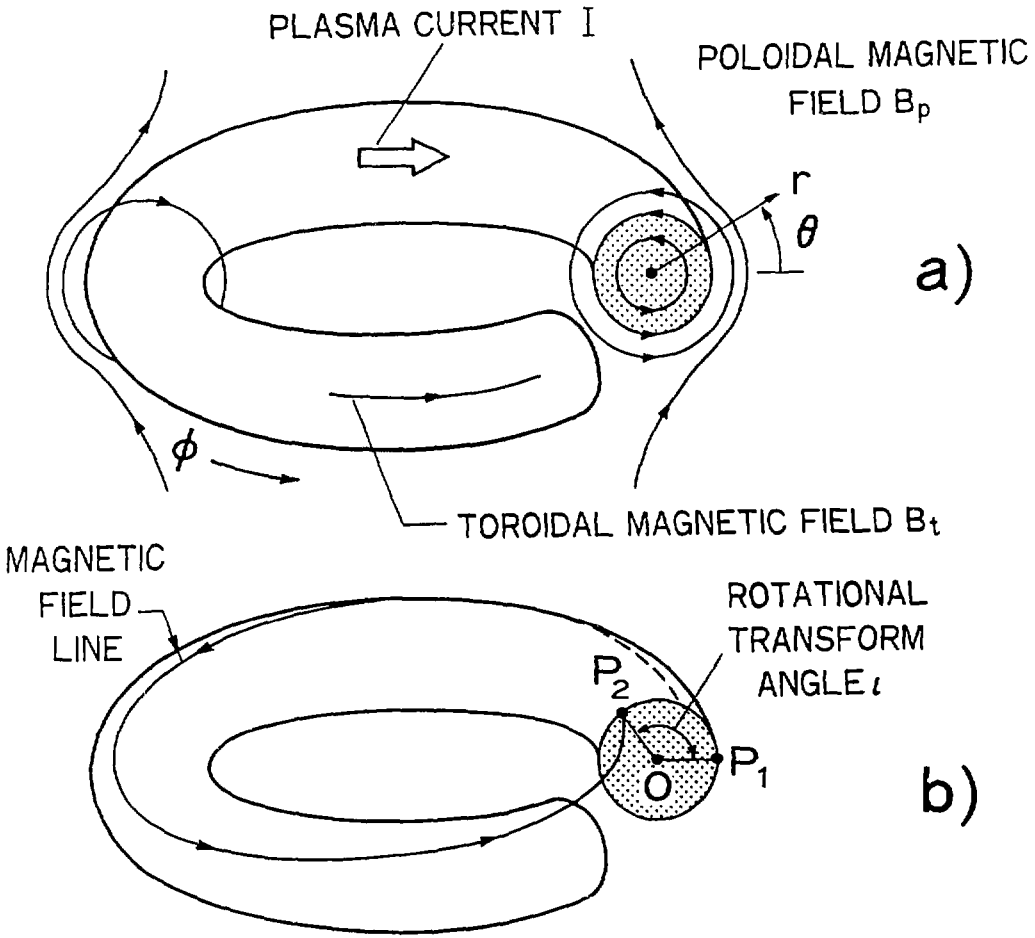
PLASMA CURRENT I
POLOIDAL MAGNETIC FIELD B_p
r
θ
a)
ϕ
TOROIDAL MAGNETIC FIELD B_t
MAGNETIC FIELD LINE
ROTATIONAL TRANSFORM ANGLE ι
P_2
O
P_1
b)

Fig. 2

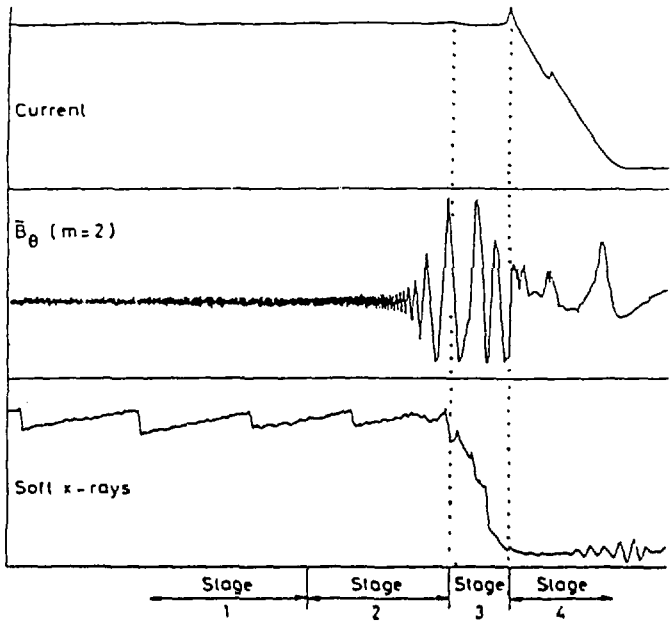
Current
$\tilde{B}_\theta$ (m=2)
Soft x-rays
Stage 1
Stage 2
Stage 3
Stage 4

Fig. 3

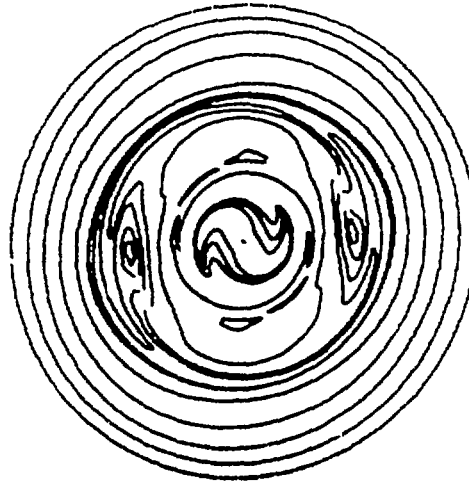

Fig. 4

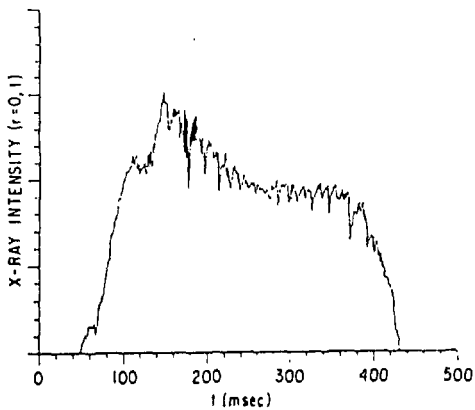

Fig. 5

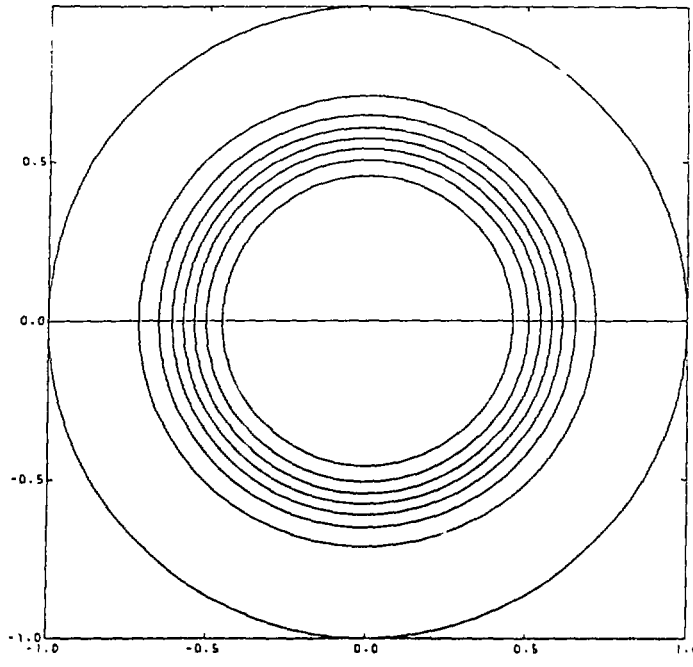

a)

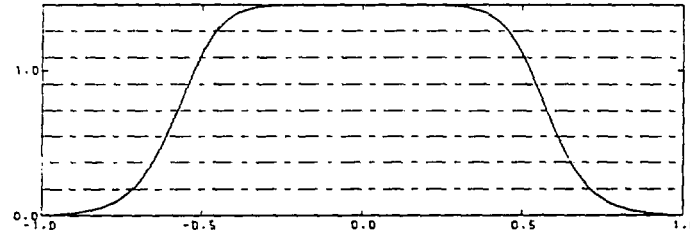

b)

Fig. 6

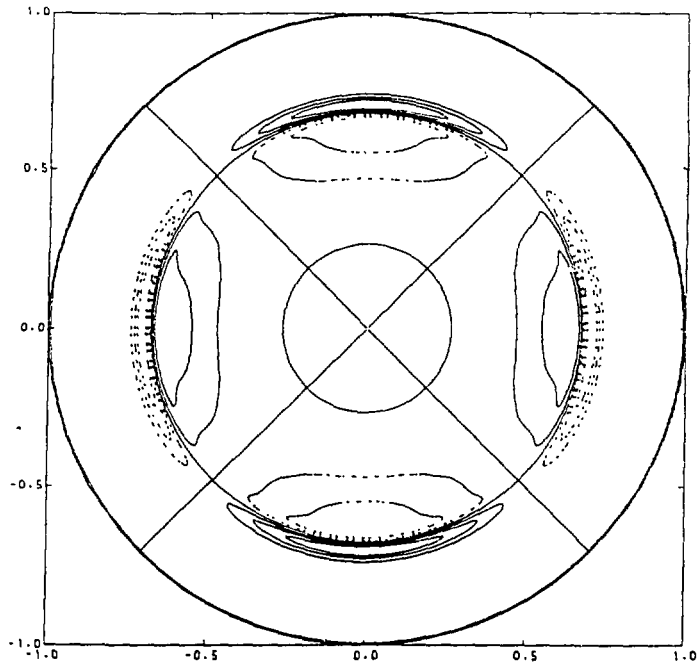

a)

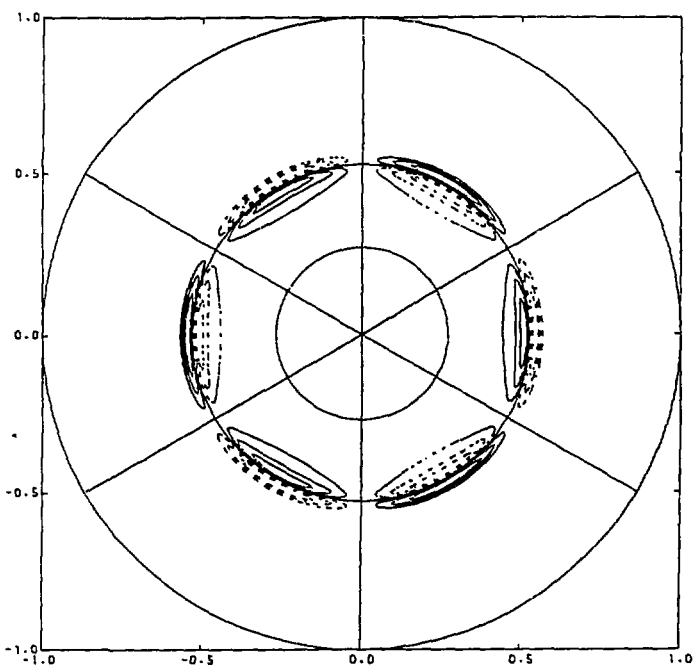

b)

Fig. 7

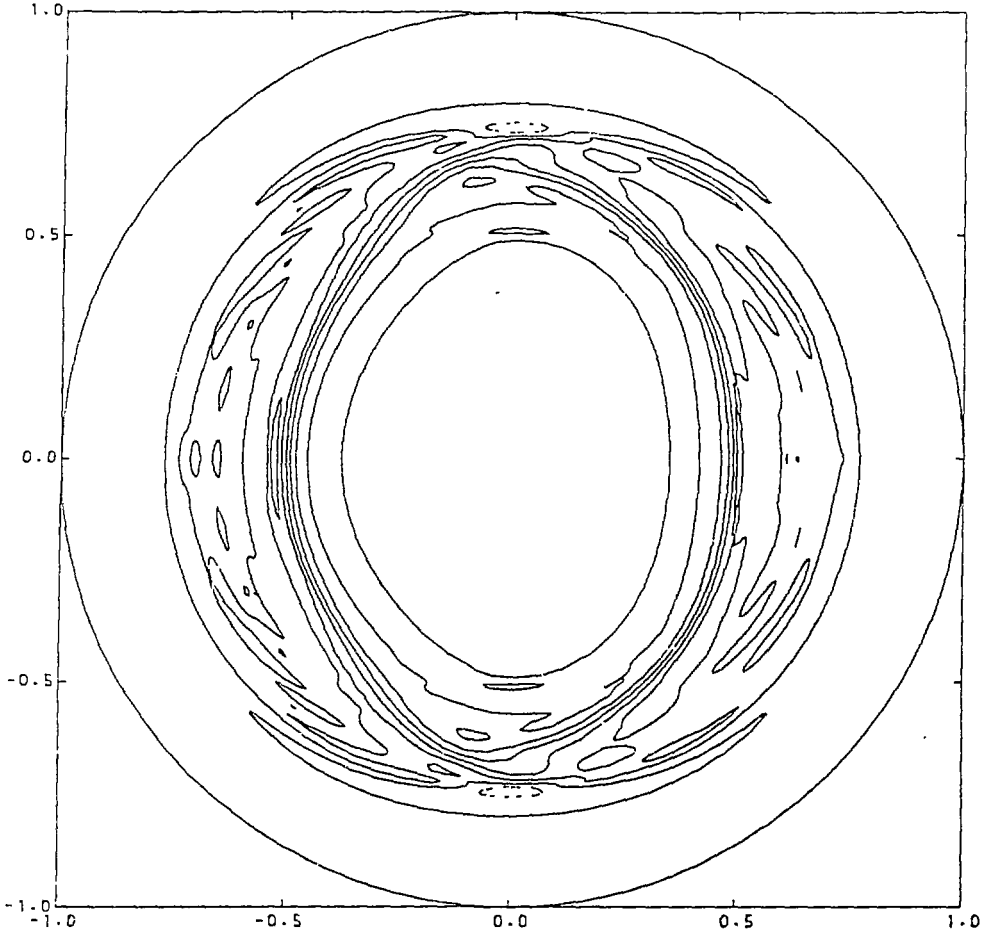

Fig. 8

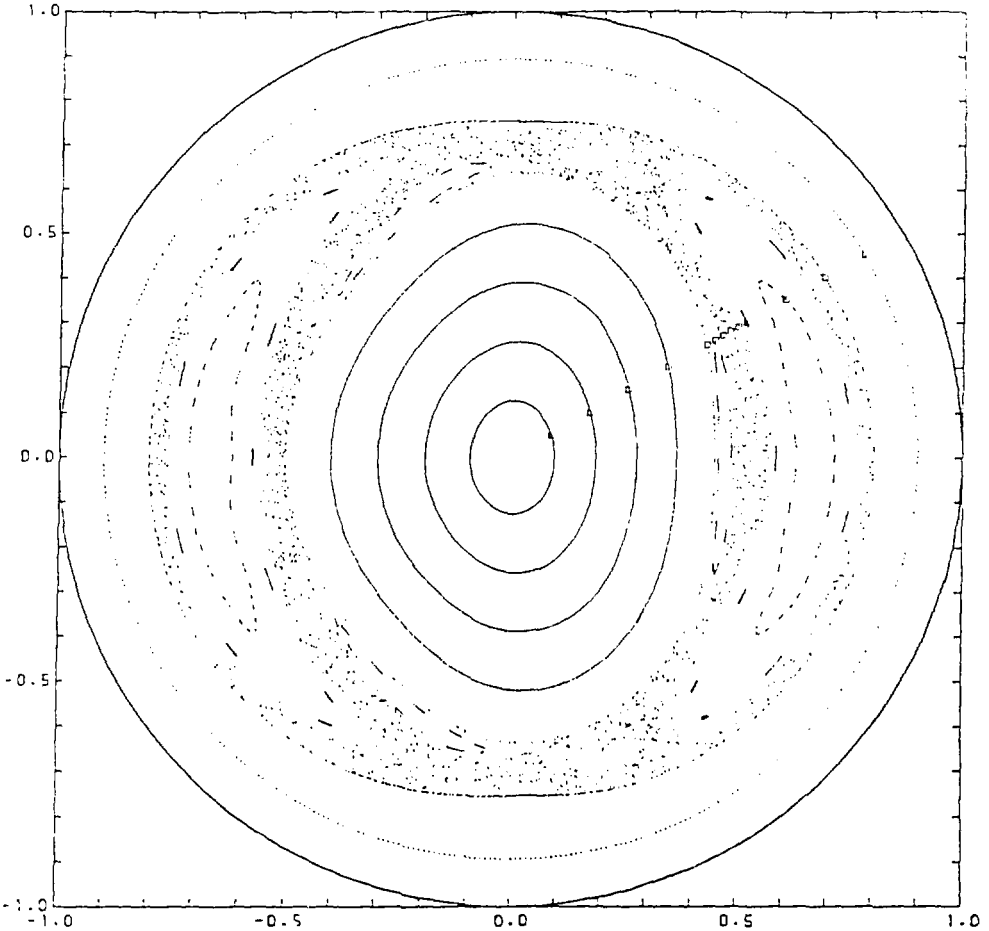

Fig. 9

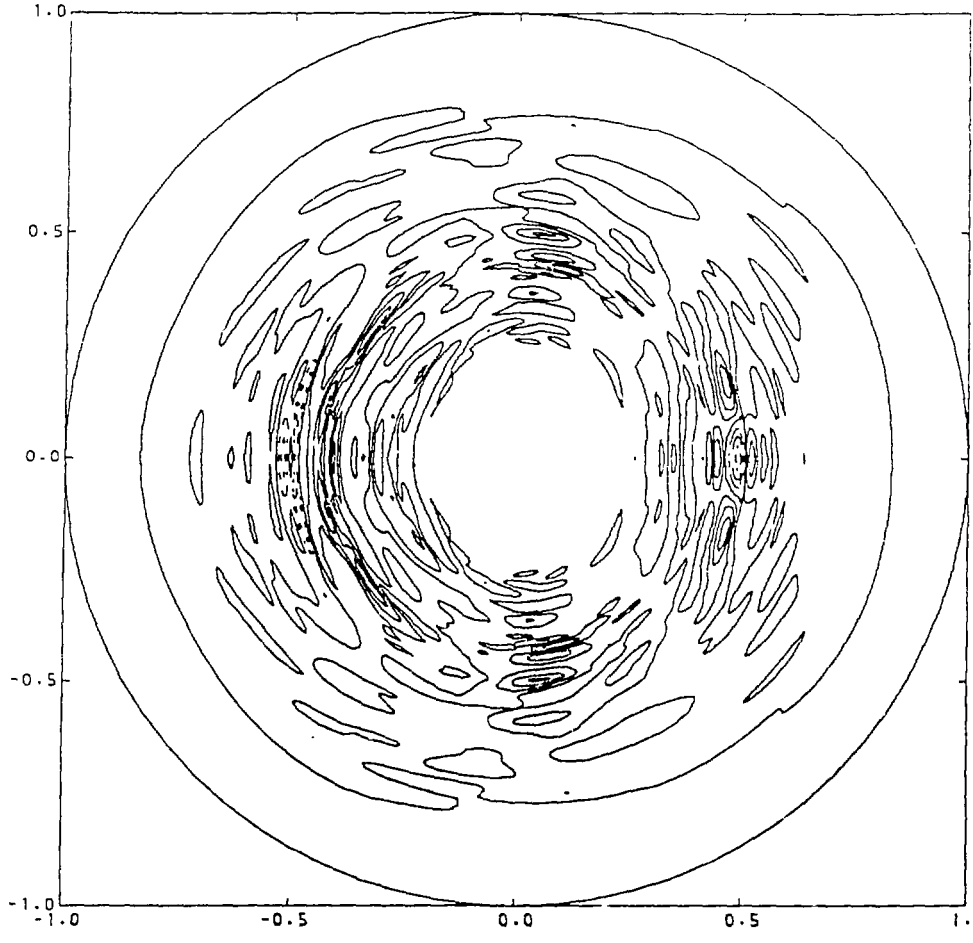

Fig. 10

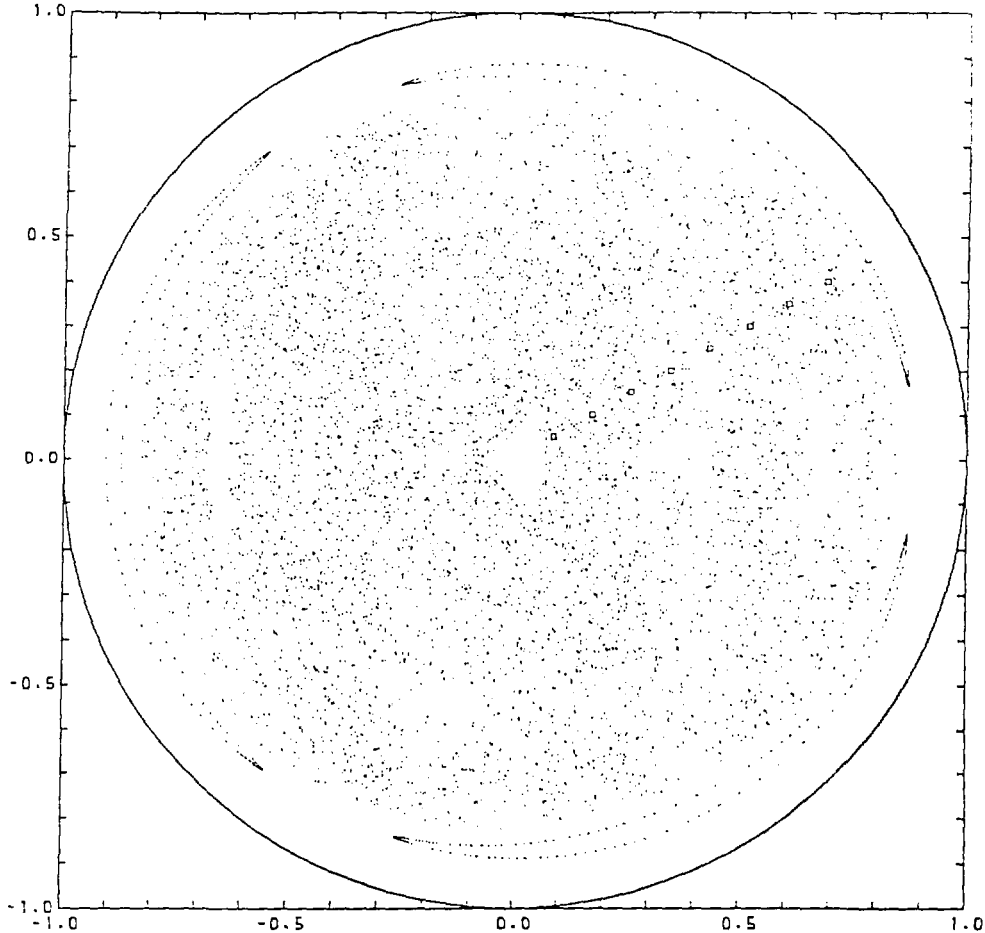

Fig. 11

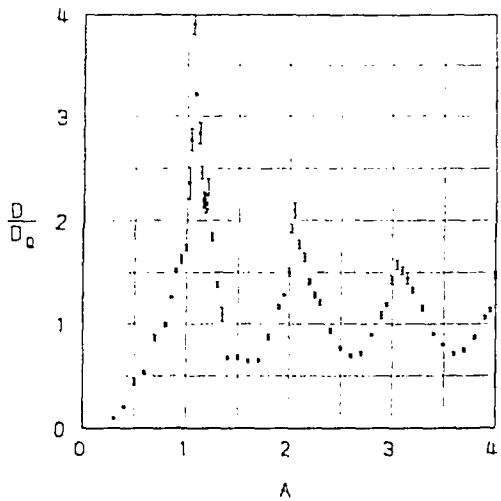

Fig. 12

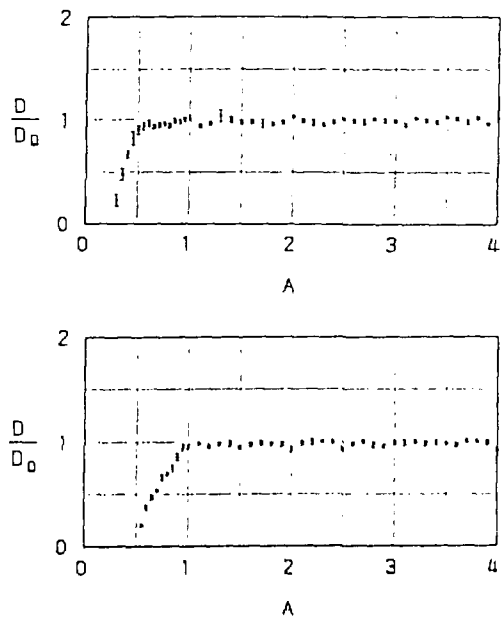

Fig. 13

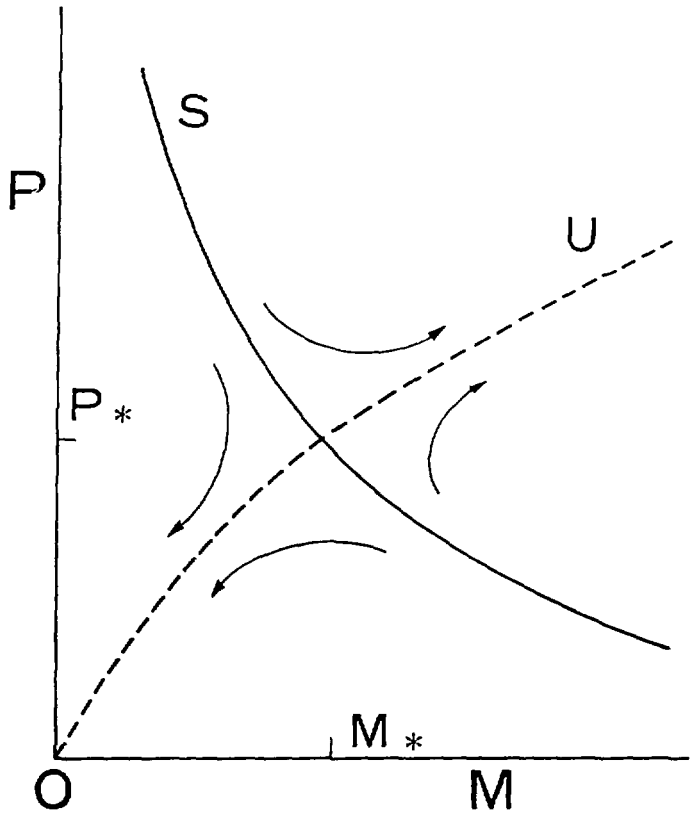

Fig. 14

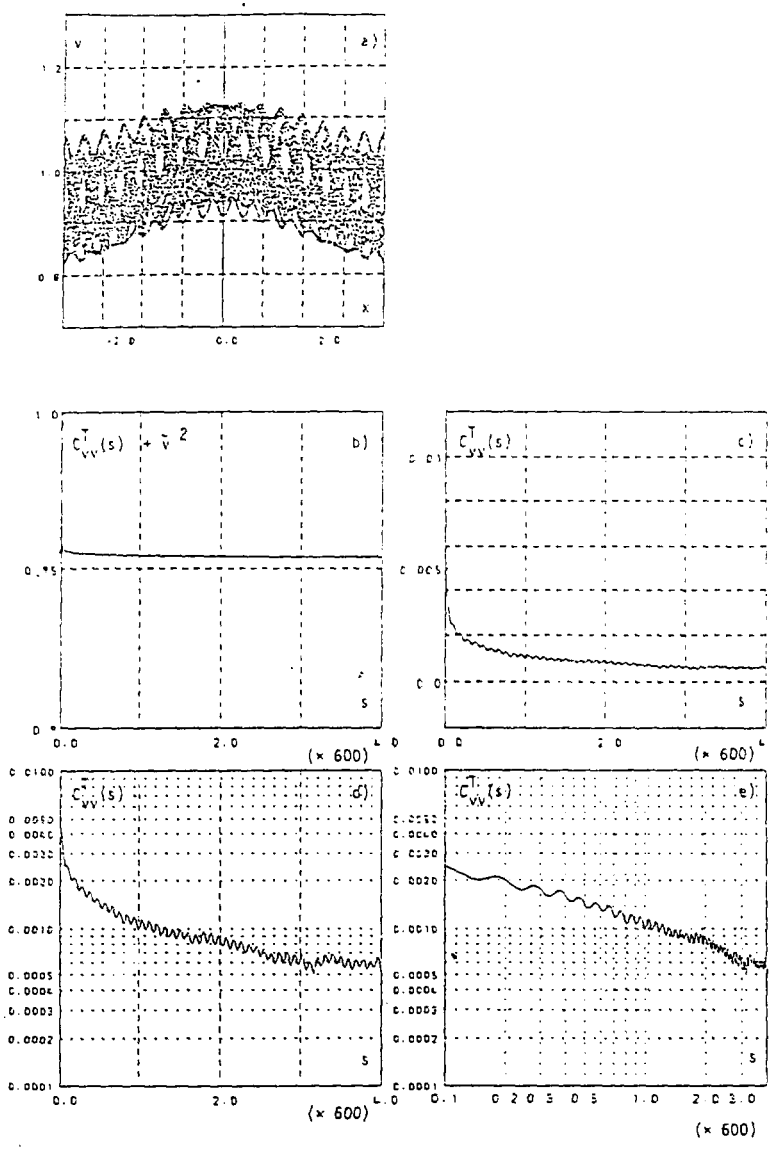

Fig. 15

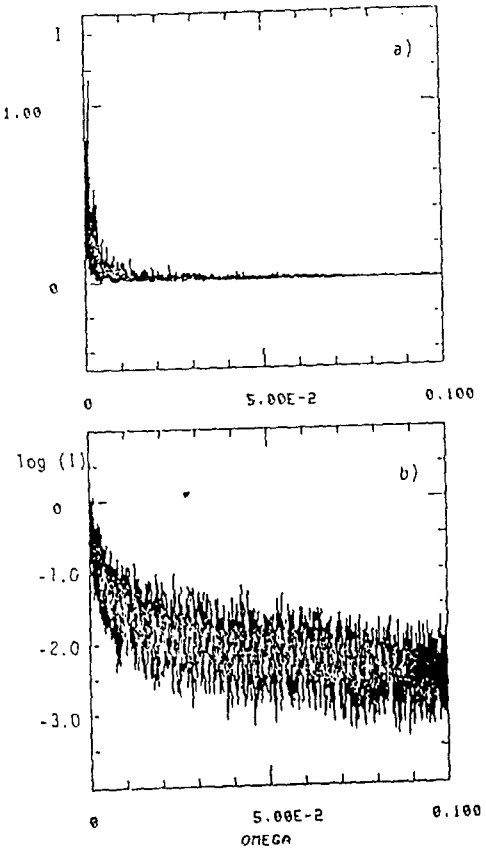
I
1.00
0
a)
0
5.00E-2
0.100
log (I)
0
-1.0
-2.0
-3.0
b)
0
5.00E-2
0.100
OMEGA
log(I)
0
-1.0
-2.0
-3.0
c)
-4.0
-3.0
-2.0
-1.0
LOG(OMEGA)

Fig. 16

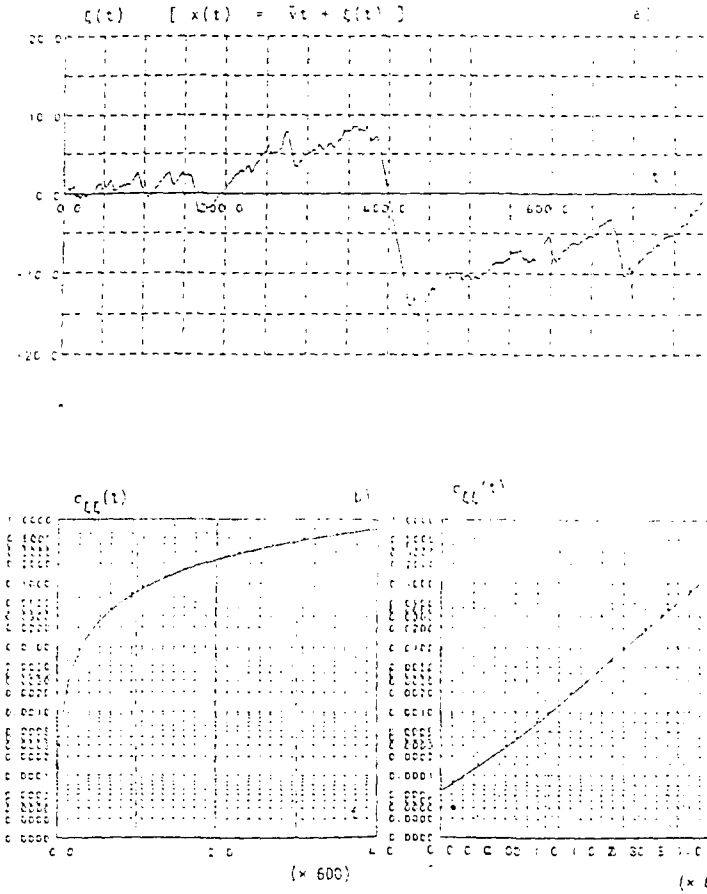

Fig. 17

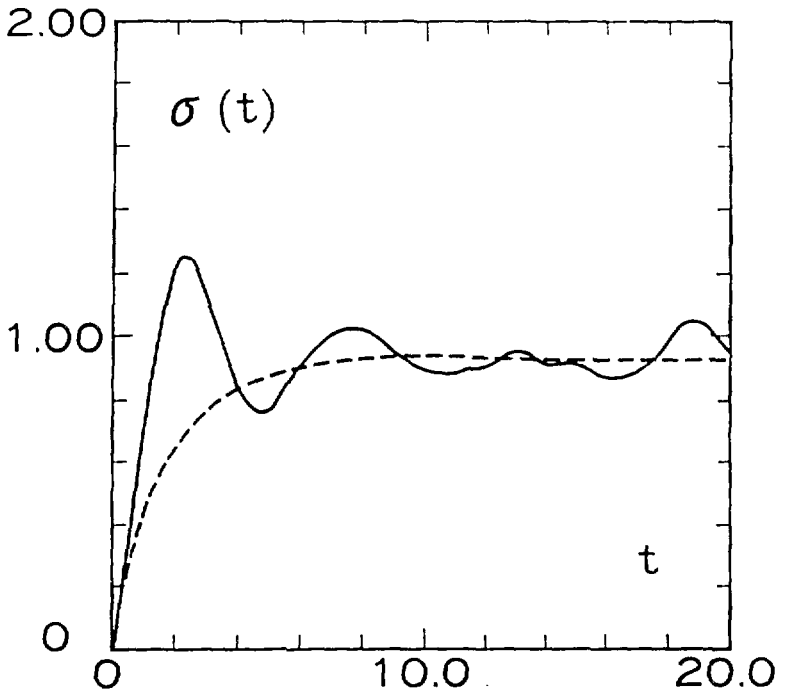

Fig. 18